



A sensitivity study of the Kelvin wave and the Madden-Julian Oscillation in aquaplanet simulations by the Naval Research Laboratory Spectral Element Atmospheric Model

Young-Joon Kim,¹ Francis X. Giraldo,² Maria Flatau,¹ Chi-Sann Liou,¹ and Melinda S. Peng¹

Received 30 January 2008; revised 7 May 2008; accepted 10 July 2008; published 16 October 2008.

[1] The dynamical core of the Naval Research Laboratory (NRL) Spectral Element Atmospheric Model (NSEAM) is coupled with full physics and used to investigate the organization and propagation of equatorial atmospheric waves under the aquaplanet conditions. The sensitivity of the model simulation to the amount of horizontal viscosity, distribution of the vertical levels, and selected details of the precipitation physics is examined and discussed mainly utilizing simulated convective precipitation with the aid of time-longitude plots and the spectral diagrams designed by Wheeler and Kiladis (1999). It is shown that the simulation of the Kelvin wave and Madden-Julian Oscillation depends strongly on the details of the vertical level distribution and the choice of parameters in the convective parameterization. Efforts are made to calibrate the new model to capture the essential interaction between the dynamics and physics of the atmosphere. The speed and spectrum of the eastward propagating Kelvin waves and the signature of the Madden-Julian Oscillation simulated by the new model reveal main features similar to those predicted by the simplified theory and found in limited observations. This study attempts to understand the significant variability found among the aquaplanet simulations by various global atmospheric models and highlights the uncertainties concerning convective processes and their coupling to large-scale wave motion in large-scale models of the atmosphere.

Citation: Kim, Y.-J., F. X. Giraldo, M. Flatau, C.-S. Liou, and M. S. Peng (2008), A sensitivity study of the Kelvin wave and the Madden-Julian Oscillation in aquaplanet simulations by the Naval Research Laboratory Spectral Element Atmospheric Model, *J. Geophys. Res.*, 113, D20102, doi:10.1029/2008JD009887.

1. Introduction

[2] The U.S. Navy has developed a new high-accuracy global atmospheric model, which scales efficiently on current and future state-of-the-art computing platforms: the Naval Research Laboratory (NRL) Spectral Element Atmospheric Model, or NSEAM. Its dynamical core [Giraldo and Rosmond, 2004; Giraldo, 2005] is based on the “spectral element” method projected to three-dimensional Cartesian coordinates, which effectively eliminates the pole singularity problem of spherical coordinates and combines the local domain decomposition property of finite element methods with the high-order accuracy of spectral transform methods.

[3] An important advantage of spectral element (SE) models is that the solution of the global matrix problem required by the semi-implicit method is straightforward and computationally efficient for either the hydrostatic or nonhydrostatic equations. The semi-implicit method for either

an SE or spherical harmonics (SH) model requires the solution of a three-dimensional Helmholtz operator. However, the only reason why SH models are competitive with SE models (or grid point models for that matter) for the hydrostatic equations is that SH models do not require the solution of a matrix problem (the Helmholtz operator is solved exactly for constant coefficients). Still, SE/grid point models are competitive with SH models at high resolution and on distributed memory architectures. In the nonhydrostatic case, the SH models now require the inversion of a matrix which adds additional computational cost to the model. The SE models, on the other hand, already include this overhead and thus transitioning to a nonhydrostatic system incurs only minimal additional computational cost.

[4] NSEAM can adopt any horizontal model grid, fixed or variable, and various time integrators such as Eulerian [Giraldo and Rosmond, 2004], semi-implicit [Giraldo, 2005], or hybrid Eulerian-Lagrangian semi-implicit [Giraldo, 2006] methods. Its spectral element formulation maintains the high-order accuracy of spherical harmonics that the current Navy’s global atmospheric model is based on, while it offers flexibility to employ any form of variable grid to enhance horizontal grid resolutions in strategic regions. Its dynamical core scales efficiently, i.e., allows the use of large numbers of processors, and was validated

¹Naval Research Laboratory, Monterey, California, USA.

²Department of Applied Mathematics, Naval Postgraduate School, Monterey, California, USA.

Report Documentation Page			<i>Form Approved OMB No. 0704-0188</i>	
<p>Public reporting burden for the collection of information is estimated to average 1 hour per response, including the time for reviewing instructions, searching existing data sources, gathering and maintaining the data needed, and completing and reviewing the collection of information. Send comments regarding this burden estimate or any other aspect of this collection of information, including suggestions for reducing this burden, to Washington Headquarters Services, Directorate for Information Operations and Reports, 1215 Jefferson Davis Highway, Suite 1204, Arlington VA 22202-4302. Respondents should be aware that notwithstanding any other provision of law, no person shall be subject to a penalty for failing to comply with a collection of information if it does not display a currently valid OMB control number.</p>				
1. REPORT DATE MAY 2008	2. REPORT TYPE	3. DATES COVERED 00-00-2008 to 00-00-2008		
4. TITLE AND SUBTITLE A sensitivity study of the Kelvin wave and the Madden-Julian Oscillation in aquaplanet simulations by the Naval Research Laboratory Spectral Element Atmospheric Model				
5a. CONTRACT NUMBER				
5b. GRANT NUMBER				
5c. PROGRAM ELEMENT NUMBER				
6. AUTHOR(S)				
5d. PROJECT NUMBER				
5e. TASK NUMBER				
5f. WORK UNIT NUMBER				
7. PERFORMING ORGANIZATION NAME(S) AND ADDRESS(ES) Naval Postgraduate School, Department of Applied Mathematics, Monterey, CA, 93943				
8. PERFORMING ORGANIZATION REPORT NUMBER				
9. SPONSORING/MONITORING AGENCY NAME(S) AND ADDRESS(ES)				
10. SPONSOR/MONITOR'S ACRONYM(S)				
11. SPONSOR/MONITOR'S REPORT NUMBER(S)				
12. DISTRIBUTION/AVAILABILITY STATEMENT Approved for public release; distribution unlimited				
13. SUPPLEMENTARY NOTES				
14. ABSTRACT				
15. SUBJECT TERMS				
16. SECURITY CLASSIFICATION OF:			17. LIMITATION OF ABSTRACT Same as Report (SAR)	18. NUMBER OF PAGES 16
a. REPORT unclassified	b. ABSTRACT unclassified	c. THIS PAGE unclassified		
19a. NAME OF RESPONSIBLE PERSON				

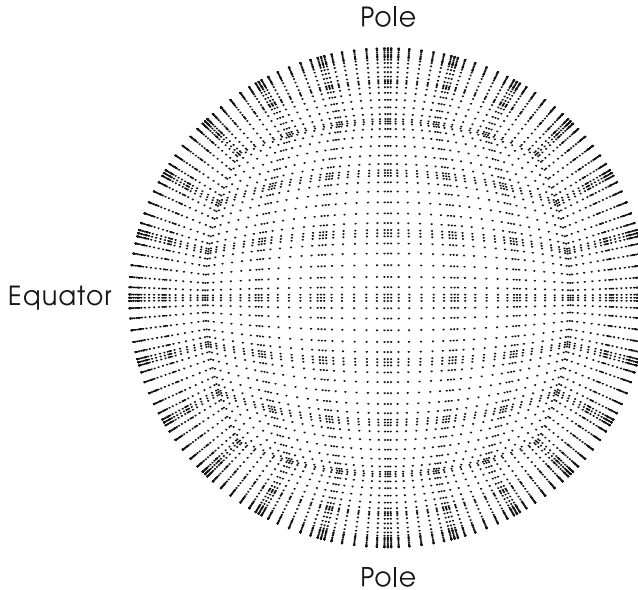


Figure 1. An orthographic view of the hexahedral grid points used in this study for NSEAM. Six elements on one face in one direction and 8th polynomial order of the basis functions are selected for this study. This horizontal resolution is roughly equivalent to the triangular spectral truncation at wave number 54 (i.e., T54) or the grid point resolution of 2.2° .

using various barotropic and baroclinic test cases [Giraldo and Rosmond, 2004; Giraldo, 2005]. The model can be discretized vertically with any grid, but the mass and energy conserving flux form of the finite difference method on the terrain-following (σ) coordinate is first selected for comparison with existing models.

[5] For this study, we modify and expand the NSEAM dynamical core to include the physics package utilized in the operational version of the Navy Operational Global Atmospheric Prediction System or NOGAPS [Hogan and Rosmond, 1991], but without the land surface parameterization (for recent model physics improvements refer to Peng *et al.* [2004], Hogan and Pauley [2007] and Kim [2007]). We select the hexahedral grid that consists of six faces of a hexahedron, each of which contains a desired number of quadrilateral elements (see Figure 1) following Giraldo and Rosmond [2004].

[6] Among various methods to validate an atmospheric model is to force the model under controlled and simplified sets of boundary and initial conditions so that the results can be interpreted in a relatively straightforward manner and also intercomparable to those of other similar models, although the correct solution is not quite known except by simplified theory and limited indirect observations. A good recent example is the aquaplanet experiments proposed by Neale and Hoskins [2001a, 2001b] in which the Earth is covered with water only. These experiments provide a useful and convenient test bed for investigating the interaction between the dynamics and physics in atmospheric models.

[7] In this study, we validate NSEAM by configuring it for aquaplanet experiments mainly following Neale and

Hoskins [2001a]. We perform various sensitivity experiments in order to understand and improve the aquaplanet simulation. Sensitivity of aquaplanet simulations to horizontal resolution was studied previously. For example, Lorant and Royer [2001] found from general circulation model (GCM) experiments that with higher resolution the convective cells are more intensified and concentrated, being accompanied by improved simulation of equatorial waves that modulate near-equatorial convection. Sensitivity of aquaplanet simulations to vertical resolution was also studied earlier. For instance, Inness *et al.* [2001] compared between 19 and 30 (unevenly spaced) layer versions of their GCM and discussed its implications for Madden-Julian Oscillation (MJO) in view of the moisture budget. They reported that the effect of convection is to moisten/dry the lower troposphere in their 19/30 layer simulations, respectively. In the present study, we investigate further sensitivity of the aquaplanet simulations to selected details of the model such as the vertical distribution, as well as the resolution, of the model levels and the way the lifting condensation level (LCL) is calculated or utilized in the context of the frequency and propagation of simulated Kelvin waves and MJO.

[8] In section 2, we outline the coupling of the NSEAM dynamical core with the NOGAPS physics including the new horizontal viscosity that replaces the original horizontal diffusion. In section 3, we describe the setup of the aquaplanet experiments and present the results of the sensitivity experiments in terms of the viscosity, vertical distribution of the model levels and some details of the precipitation physics relevant to LCL. We also discuss our efforts to simulate the Kelvin waves and MJO in this section. We end the discussion in section 4 by giving concluding remarks and a short summary of additional sensitivity experiments performed but not presented in this study. Appendix A includes the derivation of the viscosity operator.

2. NSEAM With Physics

[9] The coupling of physics with NSEAM dynamics is handled by a fractional step approach, as similarly done in NOGAPS. The process in continuous space can be denoted as

$$\frac{\partial q}{\partial t} = S_D(q) + S_P(q) \quad (1)$$

where q is any prognostic physical variable, S represents the forcing, and D and P denote dynamics and physics, respectively. We first solve

$$\frac{\partial q^*}{\partial t} = S_D(q) \quad (2)$$

and then use this new, auxiliary solution to solve

$$\frac{\partial q}{\partial t} = S_P(q^*) \quad (3)$$

which represents the forcing by physical parameterizations and is evaluated in the fine mesh, i.e., at the Legendre-Gauss-Lobatto (LGL) points.

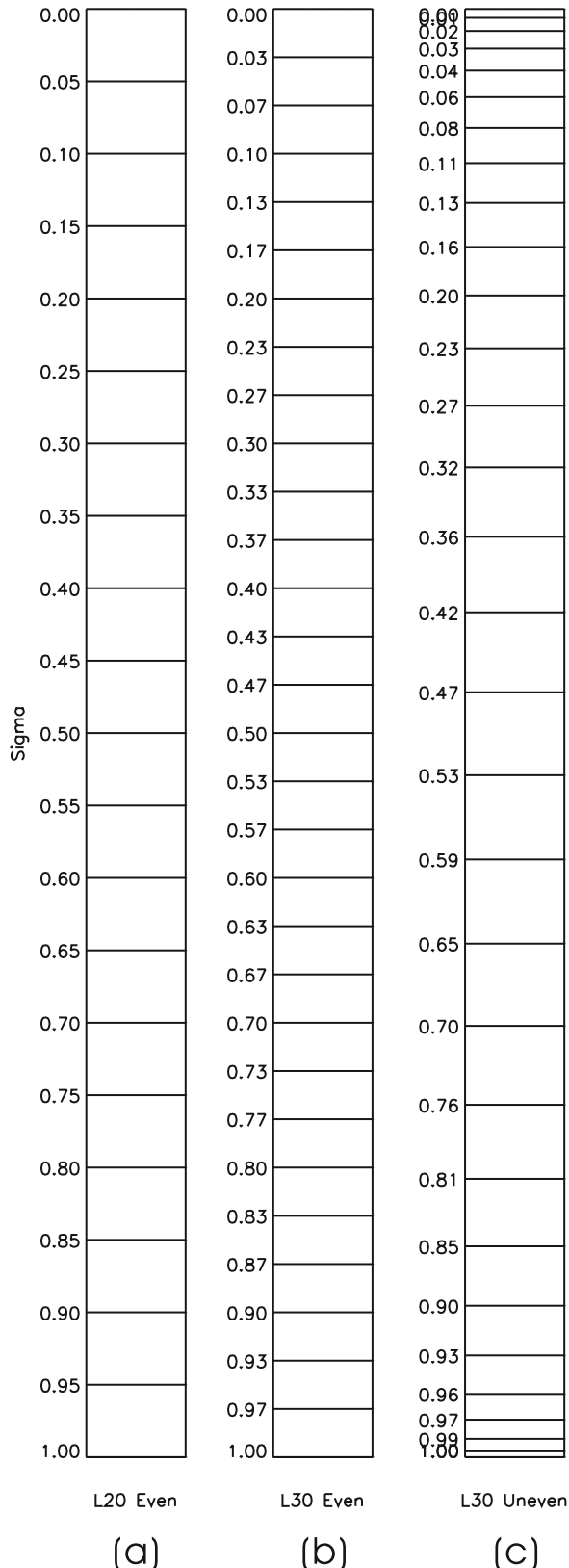


Figure 2. The vertical grids used for the NSEAM aquaplanet simulations. (a) 20 evenly spaced σ levels, (b) 30 evenly spaced σ levels, and (c) 30 unevenly spaced σ levels with tightly spaced levels near the surface and top and loosely spaced intermediate levels.

[10] We formulate a high-order hyperviscosity for physics by generalizing the low-order approach introduced by *Giraldo* [1999] as

$$\frac{\partial q}{\partial t} = S(q) + \mu \nabla^{2K} q \quad (4)$$

where K is the order of the hyperviscosity operator (in this study we choose $K = 1$, i.e., second-order), and $\mu = 1 \times 10^6$ ($\text{m}^2 \text{ s}^{-1}$) is the default viscosity value used in this study (the choice of this value will be explained in section 3.2). The expressions for the viscosity operator in equation (4) are derived in Appendix A.

[11] For the horizontal grid, we choose 6 elements on one face in one direction and 8th-order polynomial basis functions (Figure 1). The average horizontal resolution of the grid is roughly equivalent to the triangular spectral truncation at wave number 54 (i.e., T54) or the grid point resolution of 2.2° . We use 20 or 30 vertical levels, either evenly spaced or unevenly spaced in σ with the model top pressure of 1 hPa (Figure 2). The time integration is done semi-implicitly with a second-order backward difference method. The default time step is 300 s while the radiation parameterization is called every hour.

3. Aquaplanet Experiments

3.1. Experimental Setup

[12] NSEAM is configured to perform aquaplanet simulations basically following the Aquaplanet Experiment (APE) Intercomparison Project recommendations [*Neale and Hoskins*, 2001a, 2001b]: The Earth is covered with water with no orography, land or sea ice. The sea surface temperature prescribed is zonally uniform and symmetric with respect to the equator (Figure 3) as in the “control” case of *Neale and Hoskins* [2001a]. Earth eccentricity and obliquity are set to zero. The solar insolation is fixed to the equinoctial condition with the solar constant of 1365 W m^{-2} . We include the diurnal cycle in this study. CO_2 is prescribed to the amount of 348 ppmv following the Atmospheric Model Intercomparison Project (AMIP [*Gates*, 1992]) II [see also *Weare*, 2004]. The ozone is also taken from AMIP II and zonally averaged, but is symmetrized with respect to the equator for this study.

[13] Furthermore, we take the year 2005 averages of the humidity and air temperature from the National Centers for Environmental Prediction/National Center for Atmospheric Research (NCEP/NCAR) Reanalysis data [*Kalnay et al.*, 1996], which for this study are also zonally averaged and symmetrized with respect to the equator. We impose this latitudinal symmetry of the ozone, humidity and air temperature to remove the initial asymmetry so that any asymmetry that develops during simulation is due solely to the model physics. The simulations are run for 1 year with the output saved every 12 h. The first 30 days are considered a spin-up period and excluded in the averages of the 12-h interval outputs.

3.2. Sensitivity to Horizontal Viscosity

[14] Horizontal viscosity is a crude way of parameterizing the horizontal effects of turbulent mixing as well as suppressing computational noise. For idealized test cases with

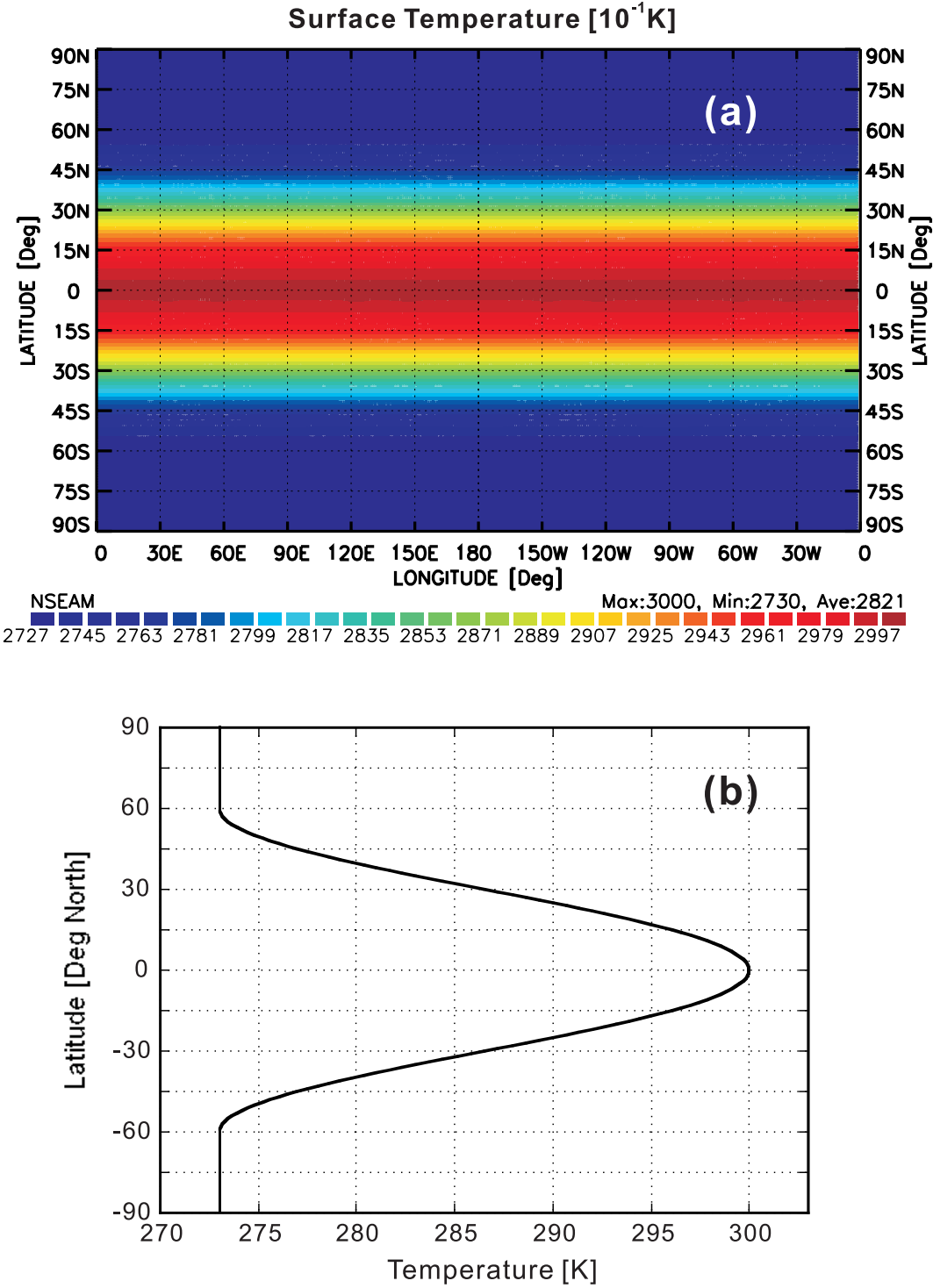


Figure 3. (a) The sea surface temperature (10^{-1} K) prescribed for the aquaplanet experiments with NSEAM, proposed for the Aquaplanet Experiment (APE) Intercomparison Project by Neale and Hoskins [2001a]. (b) The zonal mean profile of the temperature with respect to the latitude. The maximum is 300 K (27°C) over the equator and the minimum is 273 K (0°C) at the poles.

NSEAM, *Giraldo* [2005] used the viscosity coefficient of $\mu = 7 \times 10^5 \text{ m}^2 \text{ s}^{-1}$, based on the suggestion by *Polvani et al.* [2004] for baroclinic instability waves. In this study, we experiment a range of viscosity values with its maximum guided by this value. We perform a series of sensitivity experiments to determine the optimal magnitude of the

viscosity given by equation (4) with the Laplacian operator expressed by equation (A2) in Appendix A.

[15] Figure 4 presents the time-longitude (or Hovmöller) plots of the convective precipitation averaged over the equator (5°S – 5°N) for the first 90 days of the simulations with twenty evenly spaced vertical levels. We choose a

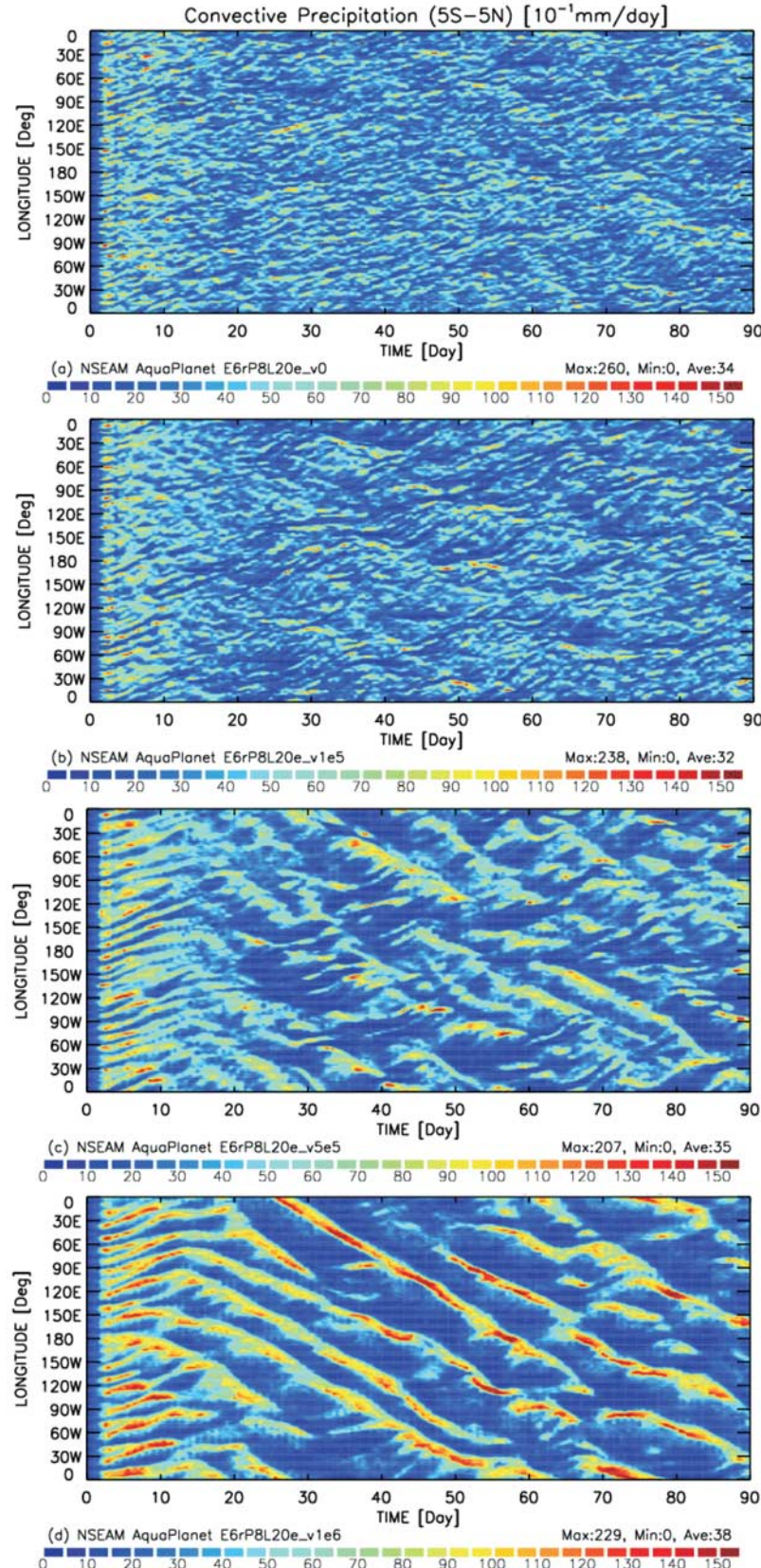


Figure 4. Time-longitude (or Hovmöller) plot from days 0 to 90 of the convective precipitation (10^{-1} mm/d) averaged for an equatorial band (5°S – 5°N) obtained from the NSEAM aquaplanet experiments with 20 evenly spaced vertical levels using the viscosity value (μ : $\text{m}^2 \text{s}^{-1}$) of (a) 0, (b) 1×10^5 , (c) 5×10^5 , and (d) 1×10^6 .

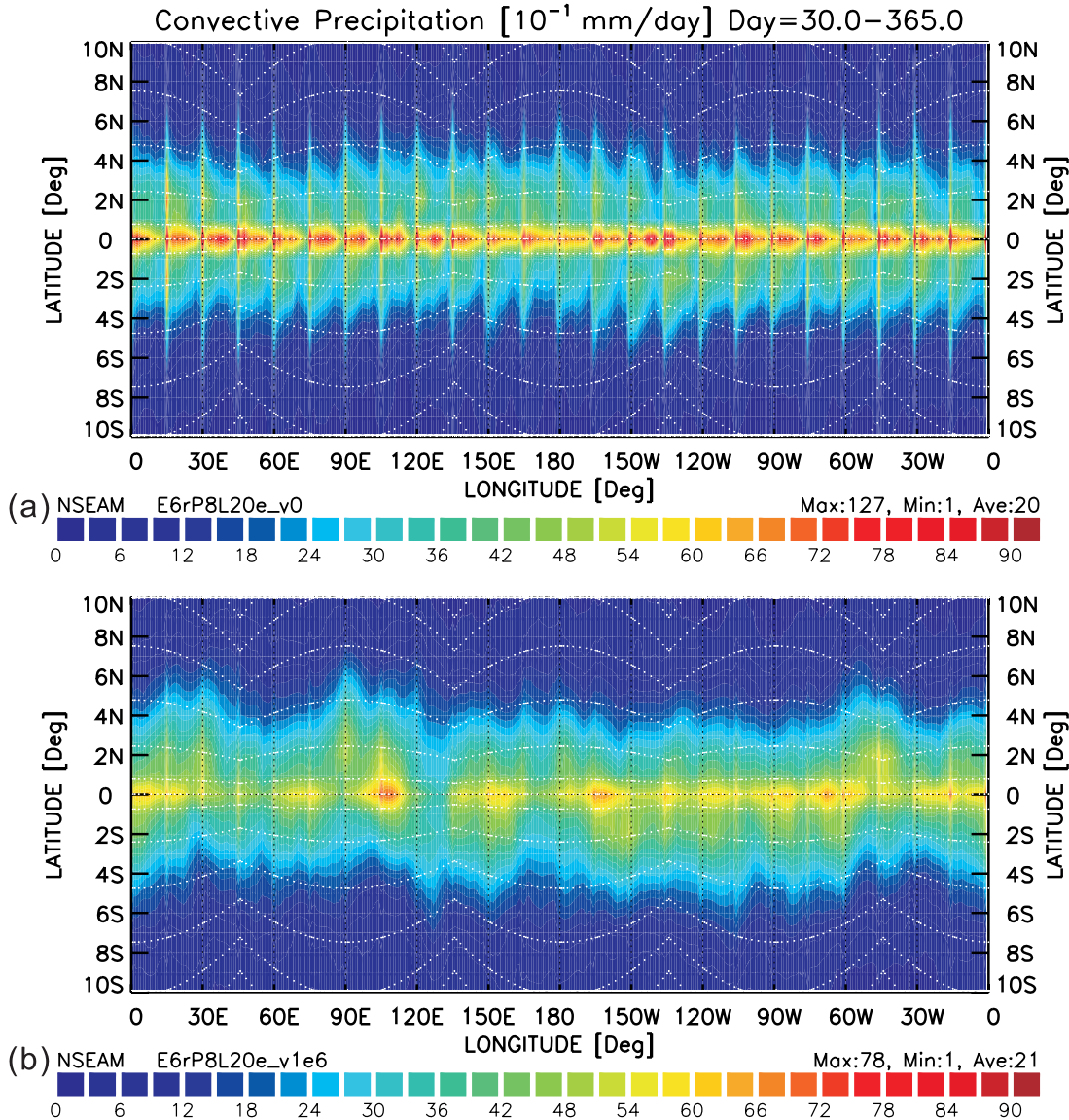


Figure 5. The convective precipitation (10^{-1} mm/d) averaged over days 30–365 from the NSEAM aquaplanet experiments with 20 evenly spaced levels using (a) no horizontal viscosity and (b) second-order viscosity of $\mu = 1 \times 10^6$ ($m^2 s^{-1}$). Superimposed are the points of the spectral element grid.

90-day interval for comparison with *Neale and Hoskins* [2001b, Figure 3a]. It is seen that after about 20 days the simulations become quite steady (not shown, but at least for 2 years). Without the viscosity (Figure 4a), the organization and grouping of precipitating convective clouds are not so pronounced. A careful look at the details, however, reveals the individual clouds (or very small clusters) propagating westward (upward and to the right in Figure 4a) whereas the loosely grouped clusters propagate eastward (downward and to the right in Figure 4a).

[16] When a small amount of viscosity is added (Figure 4b; $\mu = 1 \times 10^5$ $m^2 s^{-1}$) the clustering and propagation become somewhat more noticeable. With greater viscosity, the eastward propagation of the cloud clusters is quite evident while the westward propagation on the contrary is becoming less visible as compared in Figure 4c ($\mu = 5 \times 10^5$ $m^2 s^{-1}$) and Figure 4d ($\mu = 1 \times 10^6$ $m^2 s^{-1}$). With the larger values

(Figures 4c and 4d), the organization and propagation features are similar to those of other studies [e.g., *Neale and Hoskins*, 2001b]. Throughout the remainder of this study, we choose $\mu = 1 \times 10^6$ $m^2 s^{-1}$ as the default value for the viscosity since it produces more organized patterns in the diagnostics that will be presented later in this study.

[17] Furthermore, the SE grids suffer from a well-known problem that the horizontal grid structure becomes visible by concentrated values of a physical variable, notably the precipitation, due to the reduced grid intervals along the element boundaries. The viscosity can alleviate this “grid imprinting” phenomenon as shown in Figure 5, which compares the convective precipitation fields averaged over days 30 through 365 in an equatorial band simulated without (Figure 5a) and with (Figure 5b) using the default value of the viscosity. Similar results were found from the NCAR’s Community Atmospheric Model (CAM) with an

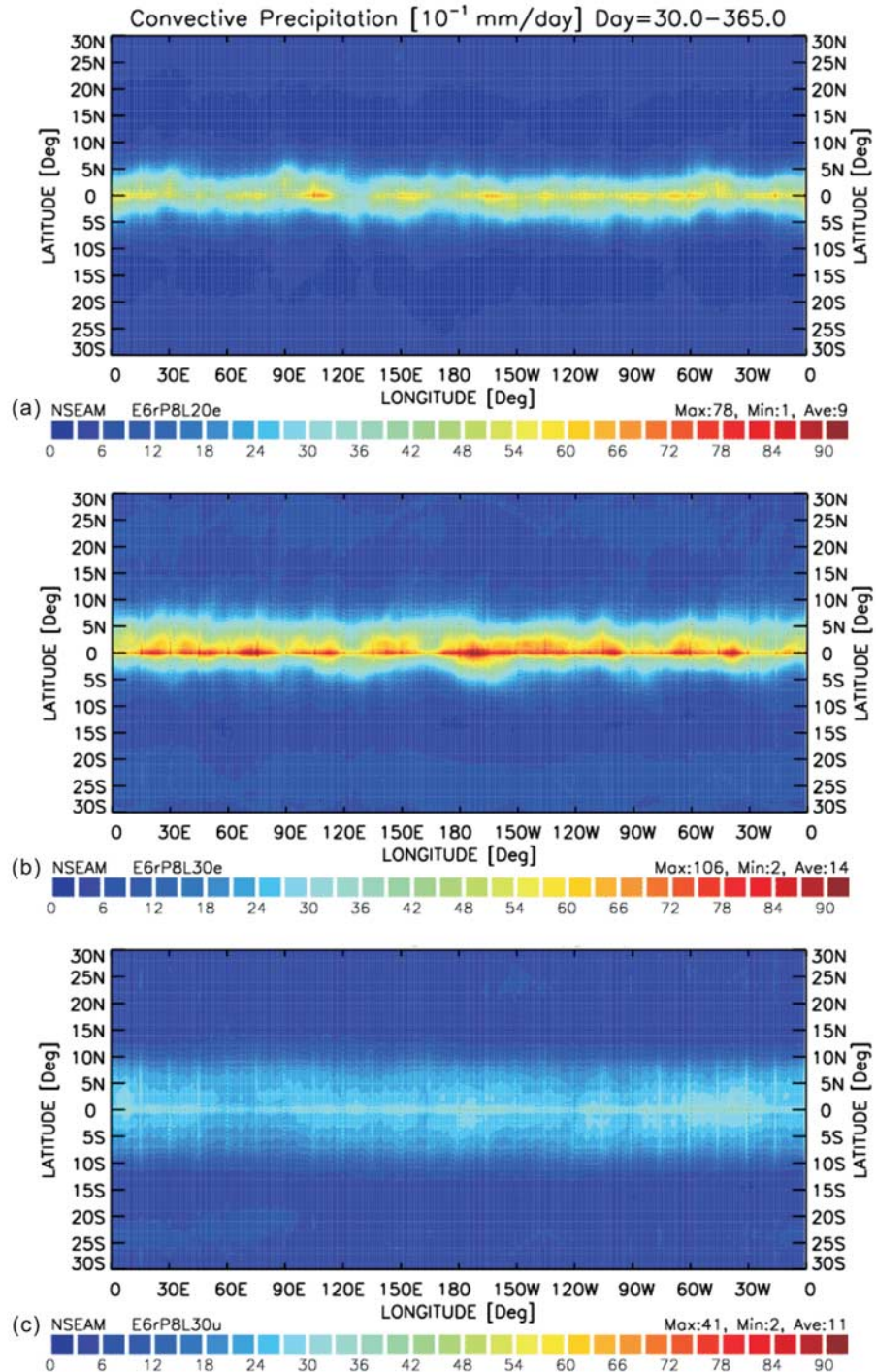


Figure 6. The convective precipitation (10^{-1} mm/d) averaged over days 30–365 from the NSEAM aquaplanet experiments with (a) 20 evenly spaced (L20e), (b) 30 evenly spaced (L30e), and (c) 30 unevenly spaced vertical levels (L30u) given in Figure 2.

SE dynamical core (M. Taylor, personal communication, 2007). These and other (not shown) sensitivity experiments suggest that the viscosity plays an important role in organizing convection.

3.3. Sensitivity to Vertical Level Distribution

[18] We now investigate the effect of the vertical structure of the model. Figure 6 compares simulated convective

precipitations from the experiments with the three distributions of the vertical grid introduced in Figure 2, which were averaged for about a year except for the startup period of the first 30 days (i.e., averaged over days 30 through 365). The evenly spaced 20 and 30 vertical level cases (L20e and L30e, hereafter; Figures 6a and 6b, respectively) reveal more concentrated precipitation over the equator than the unevenly spaced 30-level case (L30u, hereafter; Figure 6c),

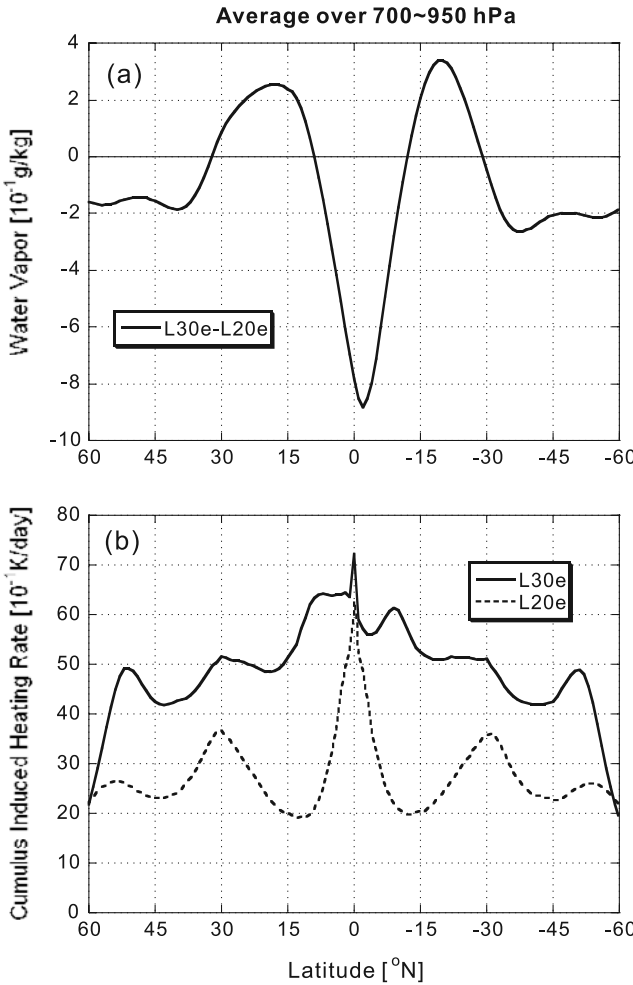


Figure 7. (a) The difference between L30e and L20e of the water vapor (10^{-1} g/kg) and (b) the comparison between L30e and L20e of the cumulus-induced heating rate (10^{-1} K/day) derived from the temperature tendency by the Emanuel convective cloud parameterization. The data have been averaged between 700 and 950 hPa over days 30–365 of the NSEAM aquaplanet simulations.

and the maximum precipitation is the greatest in L30e and the smallest in L30u.

[19] We first look into the difference between L20e and L30e (Figures 6a and 6b). With more model levels (and thus layers) in L30e, there is more precipitation along the narrow band over the equator. Figure 7a shows the difference between L30e and L20e in the amount of moisture present in the lower tropospheric model layers (averaged over 700–950 hPa that includes the LCL). The moisture over the equator in the boundary layer is greater in L20e than in L30e. This result is consistent with the finding of Inness *et al.* [2001] in that more vertical model levels (i.e., smaller vertical grid intervals) induces relative drying of the layers due to convection. Whereas the amount of moisture itself over the equator is less in L30e (Figure 7a), the moisture convergence at 850 hPa (Figure 8; represented by negative values in bluish colors) is greater in L30e (Figure 8b) than in L20e (Figure 8a). Similar results are found at nearby vertical levels (not shown). These results imply stronger

vertical moisture transfer in L30e induced by greater convergence (Figure 8b) along the equator. Therefore, the L30e grid provides more favorable condition than L20e grid for the saturation and thus condensation, leading to greater precipitation over the equatorial band (Figure 6b). Figure 7b compares the zonally averaged heating rate induced by cumulus (also averaged over 700–950 hPa for days 30–365), which is derived from the temperature tendency calculated by the Emanuel convective cloud parameterization employed in our model [Emanuel and Zivkovic-Rothman, 1999; Peng *et al.*, 2004]. The cumulus-induced heating is significantly greater in L30e over the equatorial band, which is due to the greater condensational heating associated with the stronger precipitation in L30e than in L20e.

[20] Figures 9a and 9b show the Hovmoeller plots of the convective precipitation from L20e and L30e, respectively, averaged over the equator (5°S – 5°N) from simulation day 30 to 120 (now excluding the startup period of the first 30 days). There is a clear difference between L20e (Figure 9a) and L30e (Figure 9b) in the speed of the eastward propagating waves (i.e., Kelvin waves) while the precipitation is of similar order of magnitude. With L20e it takes slightly more than two months on average for the Kelvin waves to circle the Earth along the equator, but with L30e it takes more than four months. This speed difference can be explained by an argument involving the vertical scale of the convective systems as represented by the equivalent depth and associated vertical modes under the shallow water theory. We calculate the vertical percentage distribution of convective cloud top pressures (Figure 10) as done by Inness *et al.* [2001, Figure 15] except that our calculation is from 5°S to 5°N and for every 12 h. The comparison between L20e and L30e confirms that L20e's major cloud tops (at 300 hPa) are roughly twice deeper than L30e's (at 500 hPa), which implies about twice deeper vertical scale and higher propagation speed in L20e, consistently with Figures 9a and 9b. The propagation speeds of Kelvin waves in both L20e and L30e are, however, fairly low compared with the observed atmospheric Kelvin waves [e.g., Masunaga *et al.*, 2006] and other simulations [e.g., Neale and Hoskins, 2001b; Moncrieff *et al.*, 2007].

[21] Next, we investigate the unevenly spaced 30-level case (i.e., L30u) in comparison with the evenly spaced counterpart (i.e., L30e). The moisture over the equator in the boundary layer (averaged over 700–950 hPa for days 30–365) is greater in L30u than in L30e (Figure 11a), meaning more moisture is present in the boundary layer in L30u. However, the precipitation pattern of L30u case (Figure 6c) is weaker, while broader, than L30e (Figure 6b) over the equatorial band. Rather, the difference in the precipitation is consistent with the difference in the moisture divergence between L30e (Figure 8b) and L30u (Figure 8c); that is, much weaker and broader precipitation in L30u is attributable to the much weaker and broader moisture convergence in the boundary layer. Moreover, Figure 11b shows that the cumulus-induced heating is greater in L30e than in L30u (also averaged over 700–950 hPa for days 30–365). This result is again consistent with L30e's stronger low-level moisture convergence (Figure 8b) and precipitation (Figure 6b) along the equator in view of the induced circulation in the tropics.

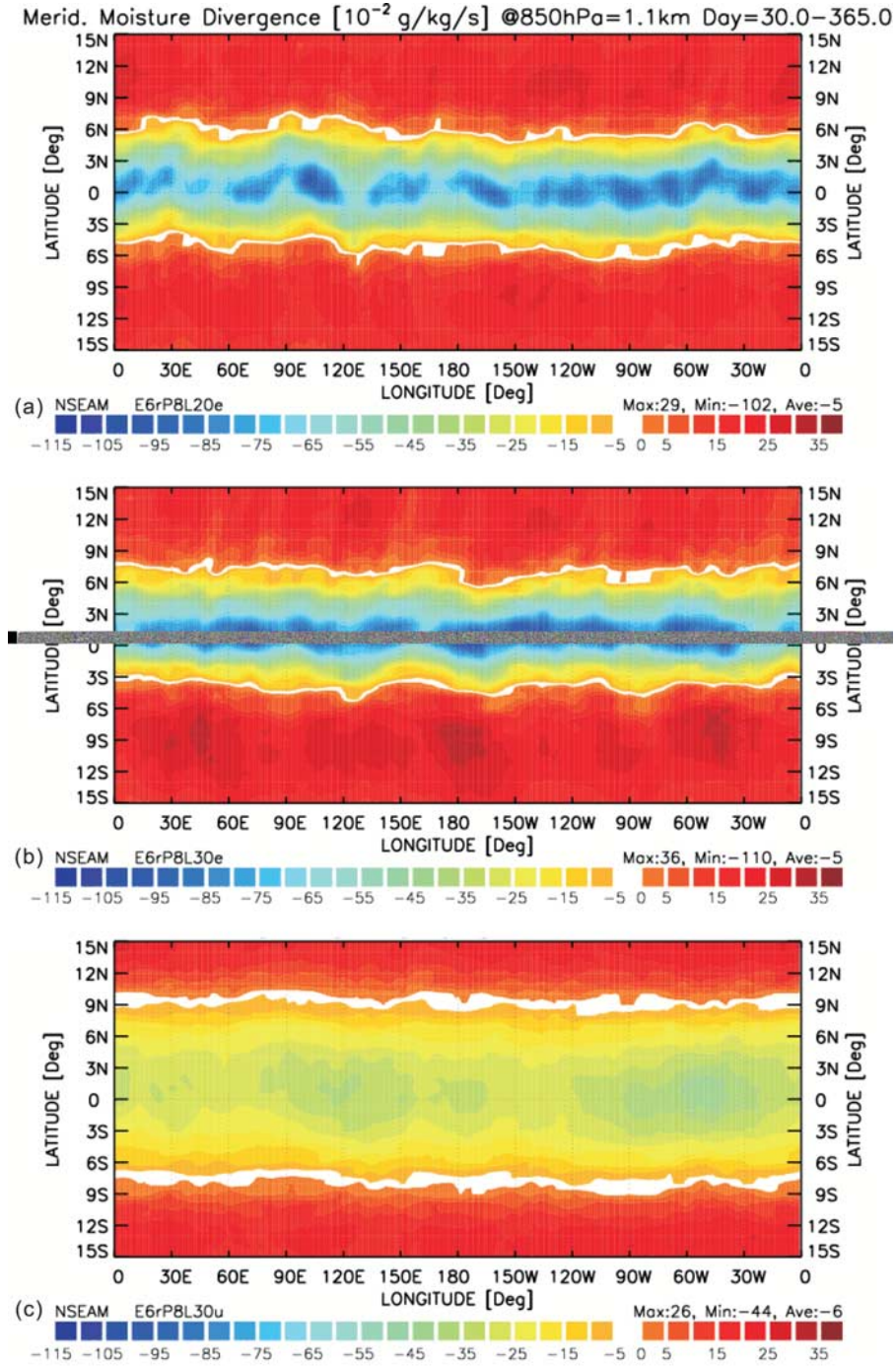


Figure 8. The meridional divergence of the moisture (10^{-2} g/kg/s) averaged over days 30–365, obtained from the NSEAM aquaplanet experiments with (a) L20e, (b) L30e, and (c) L30u vertical grid.

[22] On the other hand, from the Hovmoeller plot it is found that the Kelvin wave propagation speed for L30u (Figure 9c) is higher than that for L30e (Figure 9b) and is closer to the observed values while it is similar to that for L20e (Figure 9a). The difference in the vertical scale inferred from the cloud top distribution (Figure 10) can be linked again to this speed difference. The greater/smaller vertical scale for L30u/L30e correspond to the higher/lower Kelvin wave propagation speed for L30u (Figures 9c)/L30e (Figure 9b).

[23] As shown in this study, altering the vertical structure of the model systematically modifies the moisture budget of the boundary layer, characteristics of the convective precipitation, and distribution of the heating in clouds, thereby influencing the equivalent depth of the modeled atmosphere and propagation characteristics of the equatorial waves. As in the case with respect to L20e (Figure 7a), the smaller vertical grid intervals of L30e are associated with less moisture than L30u (Figure 11a), consistently with Inness *et al.* [2001]. Despite the less moisture present in the

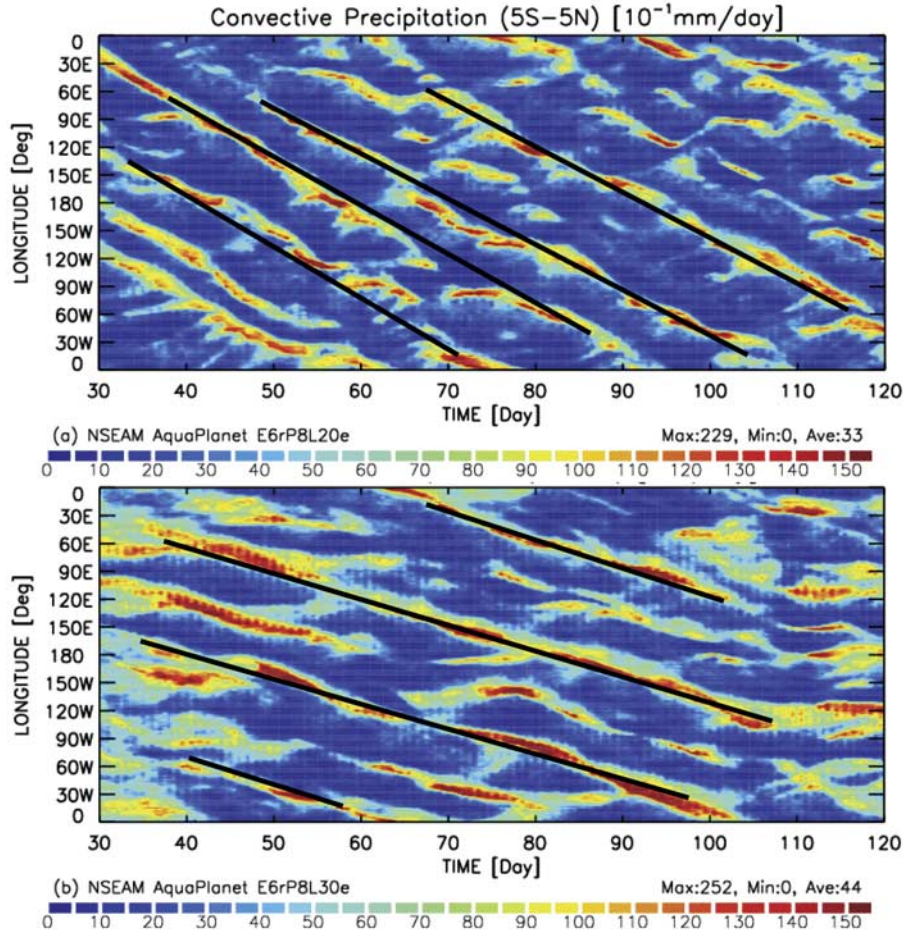


Figure 9. Time-longitude plot from days 30 to 120 of the convective precipitation (10^{-1} mm/d) averaged for an equatorial band (5°S – 5°N) obtained from the NSEAM aquaplanet experiments (a) L20e, (b) L30e, (c) L30u, (d) L30u with new LCL, and (e) L30u with modified ΔT_{max} . Note that a smaller contour interval is used for Figures 9c–9e. The solid lines are drawn to help estimate the propagation speed of cloud clusters. The dashed lines in Figures 9d and 9e are drawn to identify slower moving clusters distinguished from faster moving counterparts denoted by the solid lines.

boundary layer, however, the smaller grid intervals of L30e facilitate easier saturation of the layers and thus stronger precipitation than L30u (Figure 6) as in comparison with L20e. In the two comparisons (between L30e and L20e and between L30e and L30u), the more abundant moisture content in L20e and L30u may merely be a consequence of less precipitation than L30e.

3.4. Sensitivity to Model Precipitation Physics and Simulation of Kelvin Waves and Madden-Julian Oscillation

[24] The spectral analysis of tropical waves introduced by Wheeler and Kiladis [1999] is an effective and convenient tool for investigating the organization and propagation of equatorial waves. Figure 12 compares the (equator) symmetric component of the wave number-frequency decomposition divided by the background spectrum obtained using the simulated convective precipitation. The straight lines in Figure 12 denote the theoretical shallow water dispersion relations for linear Kelvin waves obtained without background flow and with the equivalent depths of 50 m, 25 m and 12 m based on observations and corresponding

phase speeds of 22 m/s, 16 m/s and 11 m/s (Figure 12a; respectively from left). The relatively low propagation speeds of L20e and L30e shown by the Hovmoeller plots of the convective precipitation (Figures 9a and 9b) are confirmed in Figures 12a and 12b.

[25] Here, we investigate to what extent the Kelvin wave propagation depends on details of the model physics that involve vertical motion. First, we modify the Emanuel convective parameterization so that a twice-thicker layer is used to determine the LCL. The Hovmoeller plot from this experiment with L30u is shown in Figure 9d. The rather scattered cloud clusters that were present in L30u with the old LCL formulation (Figure 9c) are now more organized with the new LCL formulation (Figure 9d) while maintaining the dominant propagation speed of the old LCL case (Figure 9c).

[26] Next, we modify the value of the specified temperature deficit at the LCL (ΔT_{max}) in the Emanuel convective cloud parameterization from 0.9 to 1.2 K. This value accounts for the subgrid turbulence within the boundary layer and its increase would enhance the chance of convection. The result (Figure 9e) displays far stronger organiza-

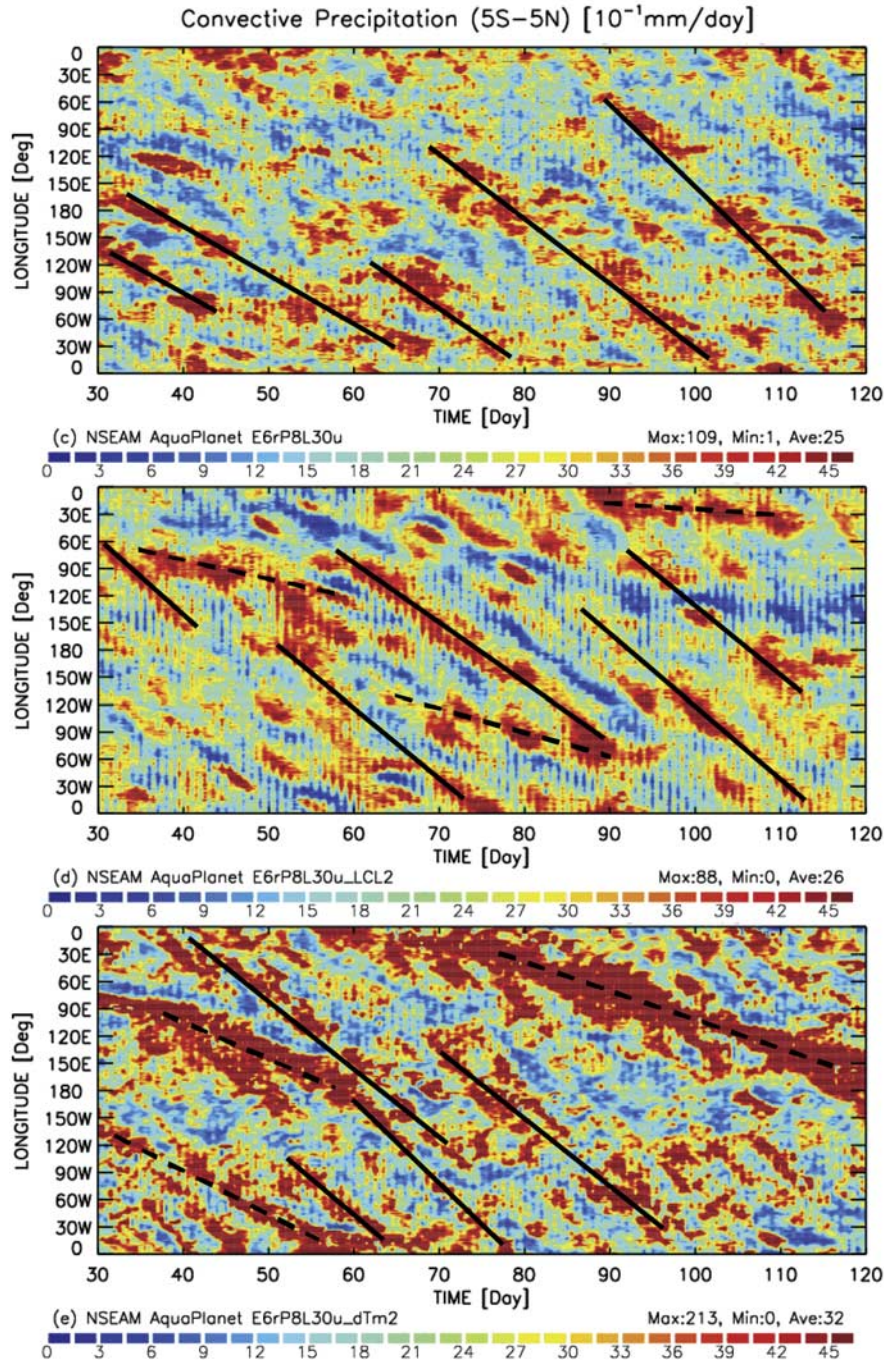


Figure 9. (continued)

tion of the cloud clusters with this change. It is interesting that increasing ΔT_{\max} amplifies the bimodal structure of the eastward propagating perturbations with the slow moving waves propagating approximately with the speed of MJO (marked by dashed lines in Figure 9e) and faster waves corresponding to observed Kelvin waves (solid lines). When the precipitation fields are filtered for the observed MJO and Kelvin wave modes (Figure 13) following Wheeler and Kiladis [1999], we can see the resemblance between the observed Kelvin and MJO modes (Figure 13a) and the simulated modified ΔT_{\max} case (Figure 13b), with more intense Kelvin waves developing during the “wet”

MJO phase (red contours in Figure 13). This relationship is not evident in other experiments presented in this study.

[27] The Wheeler-Kiladis spectral diagrams of the convective precipitation corresponding to these modified physics experiments are presented in Figures 12d and 12e. In Figures 12d and 12e, two modes can be observed: one faster mode corresponding to Kelvin waves with period of about 5–10 days and phase speeds of about 10 m/s and the other slower mode with low zonal wave numbers and periods between 30 and 50 days corresponding to observed MJO propagation characteristics. This is clearly seen as separate spectral peaks particularly in Figure 12e and, additionally,

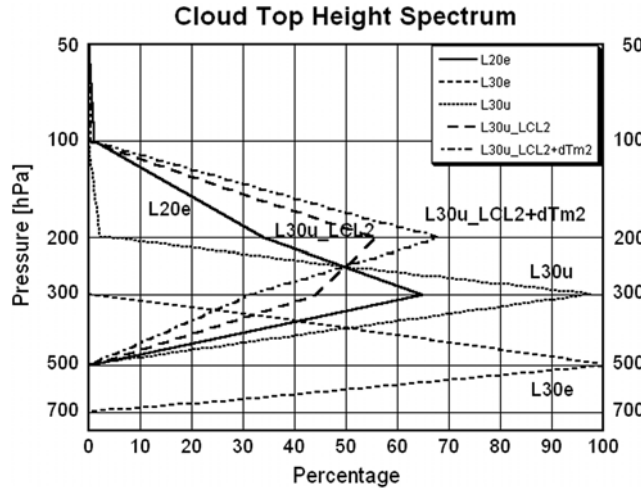


Figure 10. Vertical distribution of convective cloud top percentage for various aquaplanet simulations (see the text for details) for an equatorial band (5°S – 5°N) averaged over days 30–365. The convective cloud top in terms of the pressure in each model grid box was counted every 12 h. The ordinate (hPa) is in logarithmic scale, roughly corresponding to the elevation.

in Figure 12f that is from another experiment performed with both the modified LCL and ΔT_{\max} .

[28] The spectral peaks with periods greater than 30 days at eastward propagating wave numbers 1 and 2 are generally regarded as a signature of the MJO [Neale and Hoskins, 2001b] while higher wave numbers (3–5) are sometimes implicitly considered to fall in the MJO range (e.g., Wheeler and Kiladis [1999, Figure 3b] based on estimated outgoing longwave radiation, Masunaga *et al.* [2006, Figure 1e] based on observed deep storm cloudiness, and Cho *et al.* [2004, Figure 5d] based on observed rainfall). Our spectrum (Figure 12f, in particular), although based on the idealized aquaplanet conditions, is fairly similar to these results. In this regard, the slower moving mode, which is represented by the slower moving clusters (Figures 9d and 9e) and the low-frequency spectral peaks (Figures 12c–12f) may be associated with the MJO.

[29] We attempt to further investigate the strong spectral peak that appears at wave number 5 in the L30u_LCL2 case (Figure 12d), which is also given by Neale and Hoskins [2001b, Figure 3b] and Masunaga *et al.* [2006, Figure 1e]. From Figure 10 we find that the L30u_LCL2 case contains two cloud tops of similar percentage (200 hPa and 300 hPa) whereas L30u contains the major top at 300 hPa. The higher and lower cloud tops of L30u_LCL2 may be associated with the faster (near the theoretical lines) and slower (around 50 day period and 5E wave number) wave modes, respectively (Figure 12d). The higher cloud tops of L30u_LCL2 is taller than that of L30u, but the corresponding vertical scale is not necessarily deeper because of the secondary (lower) top at 300 hPa, which is at the same height as the major top of L30u and thus makes the two vertical scales comparable. This may be why the two cases produce relatively similar overall spectral distributions as depicted in Figures 12c and 12d. It is also noted, although not very evident, that the L30u_LCL2 case has slightly

higher percentage for the lower top at 300 hPa than the L30u_LCL2 + ΔT_{\max} case whereas it has lower percentage for the higher top at 200 hPa. The more dominant (i.e., higher percentage) lower top at 300 hPa for L30u_LCL2 may then lead to a shallower depth scale, than that would be otherwise without the lower top, which may have reduced the wave propagation speed (not shown). In this regard, the strong spectral peak of L30u_LCL2 (Figure 12d) at 5E and around 50 day period may be a result of a shallower depth scale which pushed the spectrum further toward the lower-frequency range and may thus represent a very slow Kelvin wave that is in the MJO frequency range.

[30] However, we would like to note here that our analysis based on the vertical depth scale of the convective processes, which is inferred from the vertical cloud top pressure percentage distribution, is limited and may not provide the full picture, especially because the cloud top pressures do not reflect the existence of shallower clouds under the deepest cloud within a given model column. As

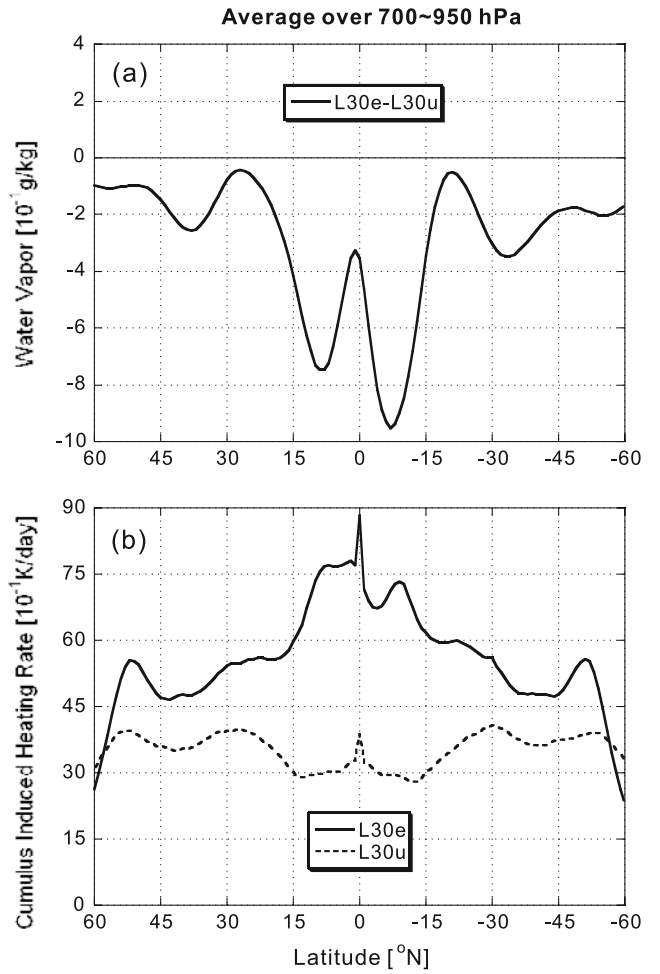


Figure 11. (a) The difference between L30e and L30u of the water vapor (10^{-1} g/kg) and (b) the comparison between L30e and L30u of the cumulus-induced heating rate (10^{-1} K/d) derived from the temperature tendency by the Emanuel convective cloud parameterization. The data have been averaged between 700 and 950 hPa over days 30–365 of the NSEAM aquaplanet simulations.

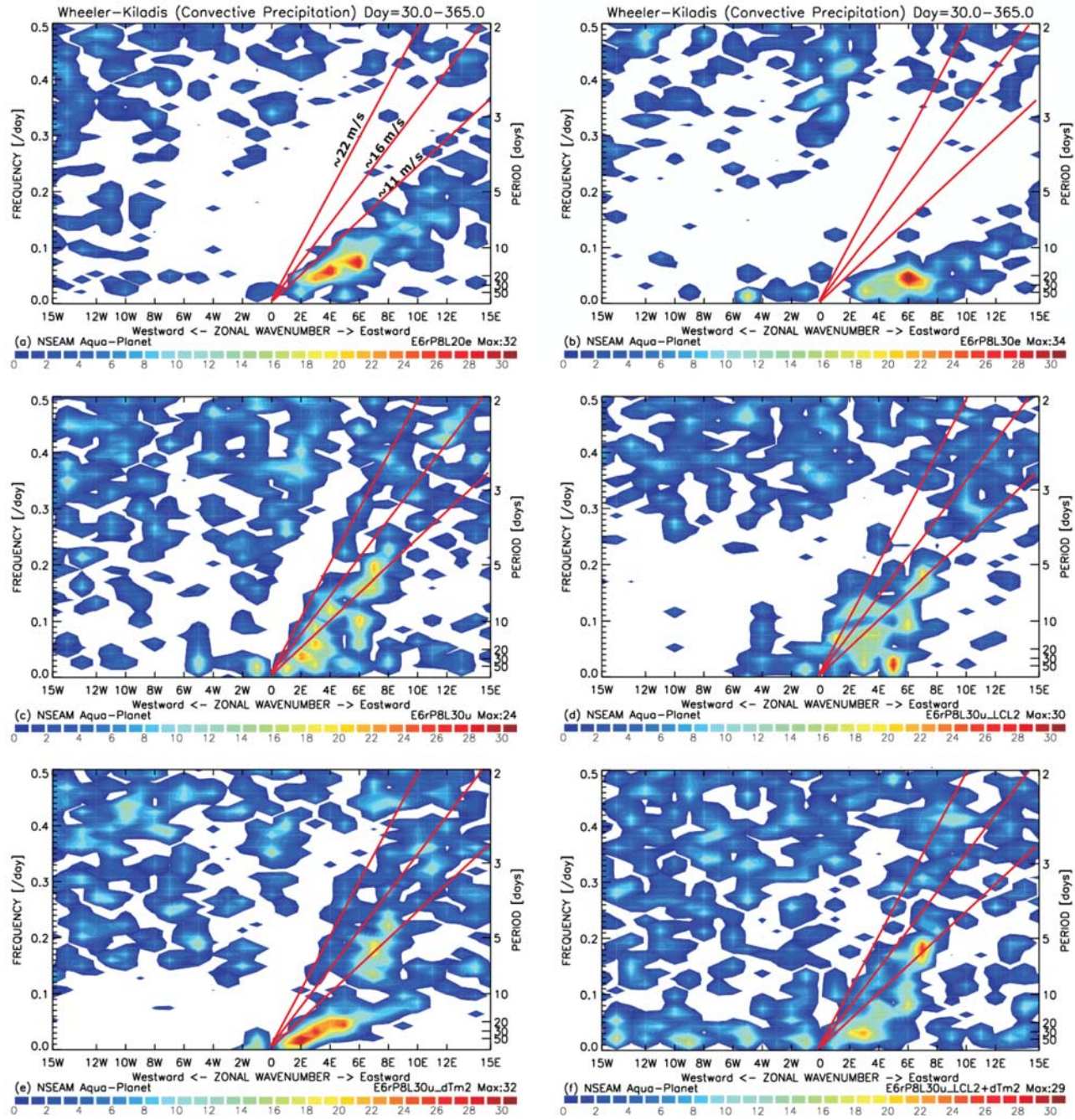


Figure 12. The symmetric component of the wave number-frequency decomposition of the convective precipitation following Wheeler and Kiladis [1999] for cases (a) L20e, (b) L30e, (c) L30u, (d) L30u with new LCL, (e) L30u with modified ΔT_{\max} , and (f) L30u with both new LCL and modified ΔT_{\max} for days 30 through 365. See the text for the descriptions of the straight lines and the speed values.

Masunaga et al. [2006] pointed out, the high-wave number MJO mode may simply have been exaggerated because of the normalization by the arbitrarily defined background spectrum and contribute to highly dispersive nature of the MJO [see also *Salby and Hendon*, 1994].

4. Conclusions and Further Remarks

[31] Even under a controlled environment of the aquaplanet experiments, the propagation of equatorial atmo-

spheric waves vary widely among models; even the simulated propagation directions of the equatorial waves are opposite in some models [see, e.g., *Moncrieff et al.*, 2007, Figure 3]. This can be due to many reasons, but the convective cloud parameterization is the prime suspect. Atmospheric models are sensitive to many details of the model, in particular to the physical parameterizations involving vertical motions of air parcels. Indeed, cumulus parameterization is considered one of the most dominant modeling components that generate uncertainties in large-

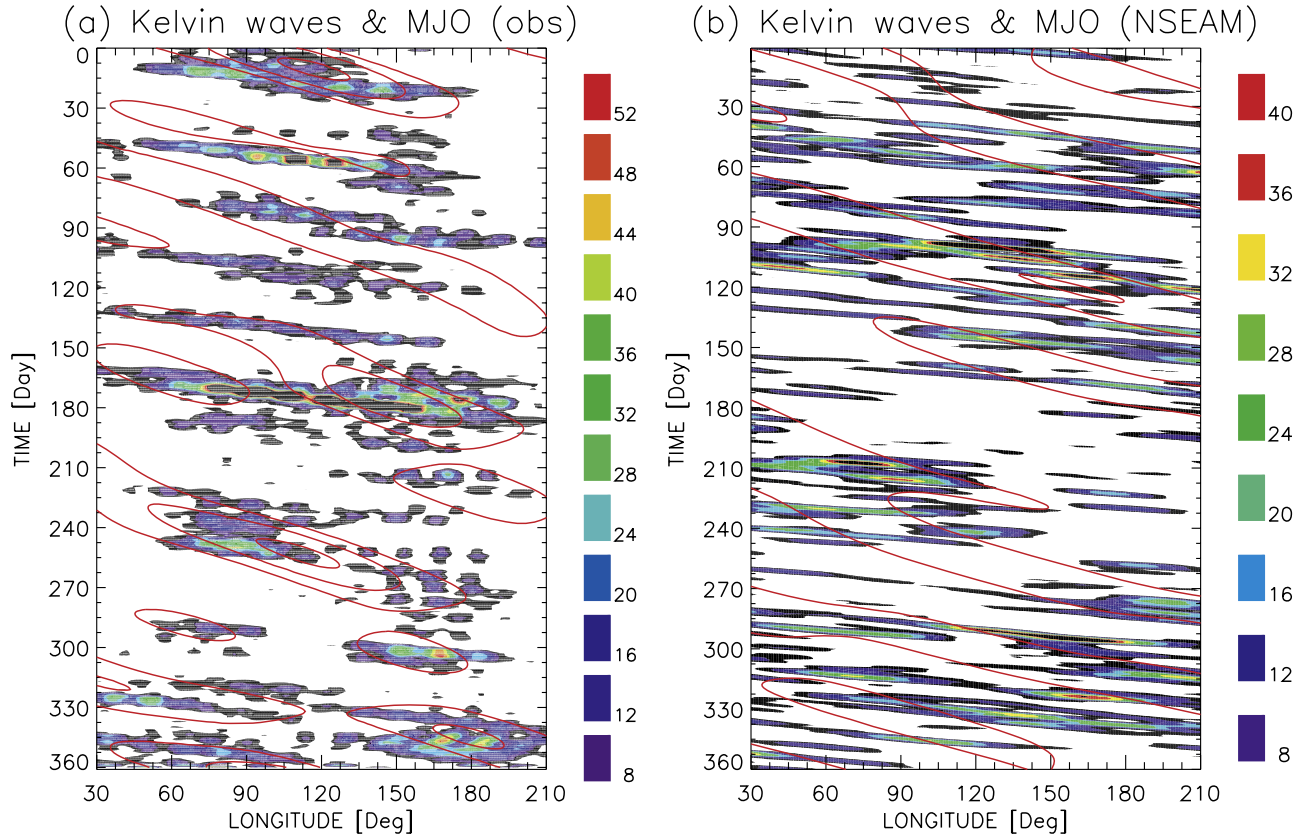


Figure 13. The powers in the convective precipitation ($(\text{mm/h})^2$) of Kelvin wave amplitude (color shades) and wet (i.e., active) phase of MJO (red contours), obtained by filtering the precipitation data in time and space [Wheeler and Kiladis, 1999]: (a) 2006 TRMM (Tropical Rainfall Measuring Mission) observation and (b) NSEAM L30u aquaplanet simulation with modified ΔT_{max} . In typical NSEAM simulations, MJO and Kelvin waves are not necessarily correlated unlike the observation shown in Figure 13a, but the observed relationship starts appearing when ΔT_{max} is increased to make it easier to trigger convection as shown in Figure 13b. Note the color shade values for Figure 13b are multiplied by 10 to facilitate the comparison with those for Figure 13a; that is, the color bar values for Figure 13b range from 0.8 to 4.

scale atmospheric simulation [e.g., Tomita *et al.*, 2005; Moncrieff *et al.*, 2007] (see also Lee *et al.* [2003] who investigated the sensitivity of aquaplanet simulations to different cumulus parameterizations, which implicitly demonstrates the uncertainties).

[32] In this study we have explored such uncertainties utilizing our new prototype global atmospheric forecast model, NSEAM. We have further demonstrated that the simulations of convective activity can be quite different even with the same convective cloud parameterization depending on the distribution of vertical levels. We have also demonstrated that the simulations are sensitive to the details of the parameterization itself such as the LCL-related processes, which modify the organization and propagation of equatorial waves. For this reason, we suggest some “standardization” of vertical levels for more direct intercomparison among the models (e.g., for the APE). While we have presented results suggesting that the new model can be calibrated to capture some basic characteristics of the Kelvin waves and MJO, the present study only provides limited analyses of the reasons for the sensitivity of the simulations to various model parameters, and mainly points

out the seriousness of the uncertainties concerning convective processes and their coupling to large-scale wave motion.

[33] Although not reported in this study, in order to further investigate the effect of the variation of the vertical resolution, we performed additional experiments by separately adding 1 or 2 more levels in L30e and removing 1 level from L30u at low levels and also by separately adding 1 or 2 more levels in L30u around $\sigma \sim 0.85$. The results were qualitatively similar to the original cases (i.e., L30e and L30u), implying that our aquaplanet simulation is not highly sensitive to a local addition or removal of one or two levels. A nonlocal, systematic modification of the layers, however, induces systematic response of the model as has been shown in this study. We investigated the dependence of the aquaplanet simulations on the integration time step (Williamson and Olson [2003] performed a comprehensive sensitivity study on this subject). In addition to the default time step of 300 s, we also tried 150 s and 450 s for L20e cases. We found from the corresponding Wheeler-Kiladis diagrams that the phase speed was proportional to the time step to some extent with the 150 s case yielding the fastest and closest to the theoretical shallow water values. We also performed a lower horizontal resolu-

tion counterpart (3 elements and 8 polynomials) of the aquaplanet experiments. Despite the lower resolution, the simulation is fairly similar to the higher-resolution counterpart, except, for example, that the precipitation band over the equator is wider and less homogeneous. While *Lorant and Royer* [2001] reported more intensified and concentrated convective cells in their higher-resolution GCM simulations, our preliminary results show less difference due possibly to the strong controlled environment of the aquaplanet conditions and the selected magnitude of the viscosity.

[34] In conclusion, the results presented in this study demonstrate that the tropical convective precipitation physics and associated equatorial wave dynamics are highly sensitive to details of the vertical structure as well as parameterized physical processes of the model. The observed sensitivity may explain the difficulties in modeling of the equatorial waves and MJO in large-scale models of the atmosphere. There exists complex interaction between the dynamics and physics in terms of the circulation around the convective area along the equator, which is likely to be underrepresented in the models. Further investigation is needed to obtain more fundamental and insightful understanding of the sensitivity and the interaction found in this study.

Appendix A: Derivation of the Second-Order Horizontal Viscosity Operator and Its Extension to High-Order Hyperviscosity

[35] A $K = 1$ hyperviscosity operator given in equation (4) can be constructed in the following way using integration by parts, based on *Giraldo* [1999];

$$\int_{\Omega} \psi \nabla^2 q \, d\Omega = \int_{\Gamma} \psi \mathbf{n} \nabla q \, d\Gamma - \int_{\Omega} \nabla \psi \nabla q \, d\Omega \quad (\text{A1})$$

where ψ represents the basis function, \mathbf{n} the normal vector, Ω refers to the interior domain and Γ to the boundaries. For a global model, periodicity is the only lateral boundary condition and, thereby, forces the first term on the right-hand side to vanish. Therefore, at discrete grid points “ i ” we can write the Laplacian operator as follows

$$\nabla^2 q_i = -M_i^{-1} L_{i,j} q_j \quad (\text{A2})$$

where “ j ” denotes neighboring points and

$$M_i = w_i |J_i|, \quad L_{i,j} = w_i |J_i| \nabla \psi_{i,j} \nabla \psi_{j,i} \quad (\text{A3})$$

are the mass and Laplacian matrices, respectively, and J is the Jacobian with corresponding quadrature weight, w . One can now extend this idea further to construct an arbitrarily high-order hyperviscosity operator as follows

$$\nabla^{2K} q_i = \left[\prod_{k=1}^K (-M_i^{-1} L_{i,j})_k \right] q_j. \quad (\text{A4})$$

[36] **Acknowledgments.** The support from the sponsor, the Office of Naval Research, under ONR Program Elements 0602435N and 0601153N is acknowledged. Comments from R. Hodur and discussions with T. Hogan

and J. Ridout are appreciated. The comprehensive comments from the anonymous reviewers were very constructive and useful. The computing time was provided jointly by the Naval Research Laboratory, Monterey, and the DoD NAVO MSRC (Naval Oceanographic Office Major Shared Resource Center) via the HPC program.

References

Cho, H.-K., K. P. Bowman, and G. R. North (2004), Equatorial waves including the Madden-Julian Oscillation in TRMM rainfall and OLR data, *J. Clim.*, **17**, 4387–4406, doi:10.1175/3215.1.

Emanuel, K. A., and M. Zivkovic-Rothman (1999), Development and evaluation of a convection scheme for use in climate models, *J. Atmos. Sci.*, **56**, 1766–1782, doi:10.1175/1520-0469(1999)056<1766:DAEOAC>2.0.CO;2.

Gates, W. L. (1992), AMIP: The Atmospheric Model Intercomparison Project, *Bull. Am. Meteorol. Soc.*, **73**, 1962–1970, doi:10.1175/1520-0477(1992)073<1962:ATAMIP>2.0.CO;2.

Giraldo, F. X. (1999), Trajectory calculations for spherical geodesic grids in Cartesian space, *Mon. Weather Rev.*, **127**, 1651–1662, doi:10.1175/1520-0493(1999)127<1651:TCFSGG>2.0.CO;2.

Giraldo, F. X. (2005), Semi-implicit time-integrators for a scalable spectral element atmospheric model, *Q. J. R. Meteorol. Soc.*, **131**, 2431–2454, doi:10.1256/qj.03.218.

Giraldo, F. X. (2006), Hybrid Eulerian-Lagrangian semi-implicit time-integrators, *Comput. Math. Appl.*, **52**, 1325–1342, doi:10.1016/j.camwa.2006.11.009.

Giraldo, F. X., and T. E. Rosmond (2004), A scalable spectral element Eulerian atmospheric model (SEE-AM) for NWP: Dynamical core tests, *Mon. Weather Rev.*, **132**, 133–153, doi:10.1175/1520-0493(2004)132<0133:ASSEEA>2.0.CO;2.

Hogan, T. F., and R. L. Pauley (2007), The impact of convective momentum transport on tropical cyclone track forecasts using the Emanuel cumulus parameterization, *Mon. Weather Rev.*, **135**, 1195–1207, doi:10.1175/MWR3365.1.

Hogan, T. F., and T. E. Rosmond (1991), The description of the Navy Operational Global Atmospheric Prediction System's spectral forecast model, *Mon. Weather Rev.*, **119**, 1786–1815, doi:10.1175/1520-0493(1991)119<1786:TDOTNO>2.0.CO;2.

Inness, P. M., J. M. Slingo, S. J. Woolnough, R. B. Neale, and V. D. Pope (2001), Organization of tropical convection in a GCM with varying vertical resolution: implications for the simulation of the Madden-Julian Oscillation, *Clim. Dyn.*, **17**, 777–793, doi:10.1007/s003820000148.

Kalnay, E., et al. (1996), The NCEP/NCAR 40-year reanalysis project, *Bull. Am. Meteorol. Soc.*, **77**, 437–471, doi:10.1175/1520-0477(1996)077<0437:TNYRP>2.0.CO;2.

Kim, Y.-J. (2007), Balance of drag between the middle and lower atmospheres in a global atmospheric forecast model, *J. Geophys. Res.*, **112**, D13104, doi:10.1029/2007JD008647.

Lee, M.-I., I.-S. Kang, and B. E. Mapes (2003), Impacts of cumulus convection parameterization on aqua-planet AGCM simulations of tropical intraseasonal variability, *J. Meteorol. Soc. Jpn.*, **81**, 963–992, doi:10.2151/jmsj.81.963.

Lorant, V., and J.-F. Royer (2001), Sensitivity of equatorial convection to horizontal resolution in aqua-planet simulations with a variable-resolution GCM, *Mon. Weather Rev.*, **129**, 2730–2745, doi:10.1175/1520-0493(2001)129<2730:SOECTH>2.0.CO;2.

Masunaga, H., T. S. L'Ecuyer, and C. D. Kummerow (2006), The Madden-Julian Oscillation recorded in early observations from the Tropical Rainfall Measuring Mission (TRMM), *J. Atmos. Sci.*, **63**, 2777–2794, doi:10.1175/JAS3783.1.

Moncrieff, M., M. A. Shapiro, J. M. Slingo, and F. Molteni (2007), Collaborative research at the intersection of weather and climate, *WMO Bull.*, **56**(3), 204–211.

Neale, R. B., and B. J. Hoskins (2001a), A standard test for AGCMs and their physical parameterizations. I: The proposal, *Atmos. Sci. Lett.*, **1**, 101–107, doi:10.1006/asle.2000.0019.

Neale, R. B., and B. J. Hoskins (2001b), A standard test for AGCMs and their physical parameterizations. II: Results for the Met Office model, *Atmos. Sci. Lett.*, **1**, 108–114, doi:10.1006/asle.2000.0020.

Peng, M. S., J. A. Ridout, and T. F. Hogan (2004), Recent modifications of the Emanuel convective scheme in the Naval Operational Global Atmospheric Prediction System, *Mon. Weather Rev.*, **132**, 1254–1268, doi:10.1175/1520-0493(2004)132<1254:RMOTEC>2.0.CO;2.

Polvani, L. M., R. K. Scott, and S. J. Thomas (2004), Numerically converged solutions of the global primitive equations for testing the dynamical core of atmospheric GCMs, *Mon. Weather Rev.*, **132**, 2539–2552, doi:10.1175/MWR2788.1.

Salby, M. L., and H. H. Hendon (1994), Intraseasonal behavior of clouds, temperature, and motion in the tropics, *J. Atmos. Sci.*, **51**, 2207–2224, doi:10.1175/1520-0469(1994)051<2207:IBOCTA>2.0.CO;2.

Tomita, H., H. Miura, S. Iga, T. Nasuno, and M. Satoh (2005), A global cloud-resolving simulation: Preliminary results from an aqua planet experiment, *Geophys. Res. Lett.*, 32, L08805, doi:10.1029/2005GL022459.

Weare, B. C. (2004), A comparison of AMIP II model cloud layer properties with ISCCP D2 estimates, *Clim. Dyn.*, 22, 281–292, doi:10.1007/s00382-003-0374-9.

Wheeler, M., and G. N. Kiladis (1999), Convectively coupled equatorial waves: Analysis of clouds and temperature in the wavenumber-frequency domain, *J. Atmos. Sci.*, 56, 374–399, doi:10.1175/1520-0469(1999)056<0374:CCEWAO>2.0.CO;2.

Williamson, D. L., and J. G. Olson (2003), Dependence of aqua-planet simulations on time step, *Q. J. R. Meteorol. Soc.*, 129, 2049–2064.

M. Flatau, Y.-J. Kim, C.-S. Liou, and M. S. Peng, Naval Research Laboratory, Monterey, CA 93943, USA. (yj.kim@nrlmry.navy.mil)

F. X. Giraldo, Department of Applied Mathematics, Naval Postgraduate School, Monterey, CA 93943, USA.